Adaptive multiscale moment method applied to the electromagnetic scattering by coastal breaking sea waves

A. Coatanhay[a*†] and Y.-M. Scolan[b]

Communicated by V. Kravchenko

The adaptive multiscale moment method (AMMM) was originally developed to solve Fredholm equation. More recently, this method has demonstrated to be effective for scattering problems. In this article, we show that AMMM is a relevant approach to model and to analyze the electromagnetic scattering by coastal breaking sea waves. The shape of breaking wave results from very nonlinear fluid mechanics and is a complex target for electromagnetic scattering. This article presents an efficient hydrodynamic model and, combined with AMMM, a global realistic numerical simulation of the electromagnetic signature induced by breaking sea waves. Copyright © 2015 John Wiley & Sons, Ltd.

Keywords: fluid mechanics; Fredholm integral equations; nonlinear sea wave; desingularized technique; conformal transformations; electromagnetic scattering; multiscale

1. Introduction

For remote sensing applications in maritime environment, a topic of key interest is the study of the interaction between electromagnetic waves (radar waves for instance) and sea surfaces. This subject has given rise to a significant body of scientific literature for 50 years and more. Many experimental studies highlighted the relations between the geometric characteristics of the sea surface and the scattered electric field. From a modeling point of view, with low wind speed conditions, offshore ocean surfaces can be easily described using linear physical models. In this case, for a remote observer, the sea surface is considered to be a statistical rough surface, and the electrical scattered field is estimated using an asymptotic approach [1, 2]. For a closer observer, numerical approaches, such as method of moments, provide accurate estimations of the scattered field [3].

Unfortunately, when the wind gets stronger or in the inshore, fluid mechanic models become far more complex because the physical phenomena are no longer linear. In particular, sea surfaces almost systematically generate breaking sea waves. Moreover, for remote sensing system, breaking waves induce very significant and complex electromagnetic scattered fields. As a consequence, a global realistic simulation that requires to tackle both aspects, fluid mechanics and electromagnetics, is really needed.

There exist different fluid mechanic models to simulate breaking waves. Nevertheless, most of them are either complex and time-consuming [4] or they are inappropriate for coastal area [5]. In this paper, we present an efficient approach to simulate a realistic coastal breaking waves. To this end, we introduce a hydrodynamic model based upon potential theory and desingularized approach [6].

Once the hydrodynamic model is well suited to our remote sensing application, the choice of an efficient electromagnetic model remains a challenging task. In fact, it is very well known that, due to high local curvature, standard method of moment does not perform well in terms of precision near the crest of breaking. The electrical field scattered by the crest is precisely of the most importance for remote sensing to identify the type of the sea waves.

In this paper, we investigate an alternative method, and we show that adaptive multiscale moment method (AMMM), originally developed to solve Fredholm integral equations, can be applied to model electromagnetic scattering. More precisely, we highlight that this multiscale approach could be of a great interest with curvilinear coordinate especially where there exist local curvatures. Finally, numerical simulations are presented, and a comparison is made with standard method of moments.

[a] Lab-STICC UMR 6285, ENSTA-Bretagne, France
[b] LBMS-DFMS EA 4325 ENSTA-Bretagne, Brest, France
* Correspondence to: Arnaud Coatanhay, ENSTA-Bretagne, 2 rue François Verny, 29806 Brest cedex 9, France.
† E-mail: arnaud.coatanhay@ensta-bretagne.fr

2. Free surface flow model in potential theory

A two-dimensional nonlinear free surface flow model is developed in potential theory. The flow is hence irrotational, and the fluid is inviscid and incompressible. Highly nonlinear waves are simulated. The computations are optimized in the sense that the numerical effort focuses on the free surface only. That makes it possible to perform parametrical study of the wave generation, and a large range of breaking wave patterns is covered.

The theoretical model is described in [6]. Only the main features are given here. The fluid domain is denoted $\Omega(t)$, its boundary is denoted $\partial\Omega(t)$, and the free surface $Fs(t)$ is a part of it. In practice, the free surface is the support of a Dirichlet condition. On the other hand, the solid and impermeable boundaries (with arbitrary shape) are the support of a Neumann condition. That is a source of difficulty to respect both type of boundary condition. In order to circumvent that difficulty, a change of variable is achieved so that there is no need to tackle the Neumann conditions. The change of variables follows from a conformal mapping of the tank domain. That is illustrated in Figure 1 for a tank where a bathymetry is introduced through the function $y = f(x)$. As a result, the image of the fluid domain is entirely contained in the upper half space. The horizontal axis is hence the image of the solid and impermeable boundaries.

The governing partial differential equation is the Laplace equation for the velocity potential ϕ. We prescribe homogeneous Neumann boundary conditions on walls because they do not move in time. On the free surface, we classically prescribe the continuity of stress (pressure) and normal velocity. The flow is modeled by using Green functions of the Laplace equation. Those singularities are located in the upper half space, and their symmetrical images with respect to the horizontal axis make it possible to implicitly prescribe the no-flux condition on that axis.

The implemented numerical scheme is composed of two techniques. In a first step, different conformal transformations are sequentially implemented, so that the solid boundaries of the fluid domain are turned into a rectilinear axis. By mirroring the free surface line with respect to this rectilinear axis, the fluid domain is closed. That is the key feature of the present model because the resulting boundary value problem is an interior Dirichlet problem, and Dirichlet boundary conditions are only prescribed on the free surface. The velocity potential is hence broken down into elementary solutions, which implicitly account for the homogeneous Neumann boundary conditions on the impermeable solid walls. This BVP reads

$$\Delta\phi = 0 \quad \text{in the fluid}, \quad \phi = e(\mathbf{M}, t) \quad \text{on the free surface}, \tag{1}$$

where t is time, $\vec{M}$ denotes the two-dimensional position of point M on the free surface, and the function e follows from the solution of the time differential system composed of kinematic and dynamic free surface boundary conditions.

As the transformation is conformal, we still solve Laplace's equation in the final coordinate system defined by the complex coordinate w. We denote F the complex potential and g the mapping function between the physical plane z and the transformed plane w. The complex potential is expressed as a summation of Green functions and their mirror images with respect to the axes of symmetry $\Im(w) = 0$ and $\Re(w) = 0$. Those fundamental solutions are the Rankine source $\log(w - \omega)$, where ω is the complex coordinate of the source. The flow is then equivalent to a distribution of sources, and the resulting velocity potential $\phi = \Re(F)$ reads

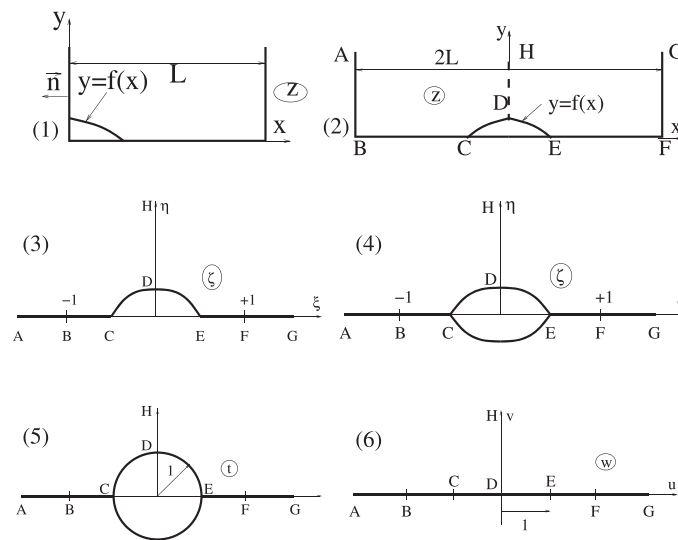$$\phi(x, y, t) = \sum_{j=1}^{N} q_j(t) G(x, y, X_j(t), Y_j(t)), \tag{2}$$

Figure 1. Successive conformal transformations used to account for a bathymetry. (1) Original physical plane, the length of the tank is L. The non horizontal bathymetry is defined by the equation $y = f(x)$ in the coordinate system $(0, \vec{x}, \vec{y})$ centered at the lower left corner. In this plane, the fluid domain is denoted $\Omega(t)$, with boundary $\partial\Omega(t)$, and the free surface $FS(t)$ is a part of it. (2) Addition of the symmetrical domain with respect to the vertical axis $x = 0$, due to symmetry, the segment DH is no longer a material boundary. (3) Domain after a Schwartz–Christoffel transformation, which turns the vertical walls into horizontal ones. (4) Addition of the symmetrical domain with respect to the horizontal axis $\eta = 0$. (5) Domain after Karman–Trefftz (corner removal procedure at points C, D, and E) and Theodorsen–Garrick transformations, which turns a near circle into a unit circle. (6) Domain after a Cayley type transformation.

where (X_j, Y_j) are the location of source number j and q_j is its strength. We denote G the complete solution for one source. The Cartesian components (U, V) of the velocity follows from

$$U - iV = \frac{dF}{dz} = \frac{dF}{dw}\frac{dw}{dz}. \tag{3}$$

The position of the sources is not arbitrary. First, we use a desingularized technique, meaning that the sources are located outside the fluid domain. Then the distance is chosen so that mass and energy are well conserved. That choice is described in [6].

The time differential system follows from the continuity of the pressure and the continuity of normal velocity written at the moving free surface. Both equations must hence be written in a Lagrangian way, and they read

$$\begin{cases} \dfrac{d\phi}{dt} = \frac{1}{2}(U^2 + V^2) - g(y - h), \\[2mm] \dfrac{dx}{dt} = U, \\[2mm] \dfrac{dy}{dt} = V, \end{cases} \tag{4}$$

where h is water depth, g is the acceleration of gravity (here, $g = 9.81 m/s^2$), d/dt is the total time derivative, and (x, y) are the Cartesian coordinates of the Lagrangian fluid particles or markers always located at the free surface. The time stepping is achieved by using a fourth order Runge–Kutta algorithm. At each intermediate step of the algorithm, the source positions are updated and their intensities as well.

In practice, we can simulate realistic breaking waves by simply starting from an initial potential energy. In addition, the effects of bathymetry help to tune the properties of the breaking wave as much as necessary. These initial conditions are rather unphysical in the sense that the free surface is initially deformed and then release starting from rest. More sophisticated initialization can be performed by using the solutions of Boussinesq equations, which are quite reliable as long as the free surface is defined by a single one to one function. Another way is to start from analytical solution such as the solitary wave given by Korteweg–de Vries equations (see [7] pp 540–542 for example). The initial free surface elevation $\eta_o(x)$ measured from the mean water level reads

$$\eta_o(x) = A\mathrm{sech}^2 b(x - x_s), \quad \text{with} \quad b = \sqrt{\frac{3A}{4h^3}} \quad \text{and} \quad \mathrm{sech} = \frac{1}{\cosh} \tag{5}$$

and x_s is the initial position of the solitary wave and its amplitude is denoted A. It is known that the subsequent free surface elevation will be

$$\eta(x, t) = A\mathrm{sech}^2 b(x - x_s - Ct), \tag{6}$$

where C is the velocity of the solitary wave, that is to say the speed of the crest of soliton as long as it propagates without changing shape along a constant bathymetry of depth h. This velocity is

$$C = \sqrt{g(h + A)}. \tag{7}$$

The velocity field (uniform along a vertical line by definition of a soliton) follows from mass conservation; it reads

$$u(x, t) = \frac{C\eta(x, t)}{h + \eta(x, t)}. \tag{8}$$

The soliton is located at $x = x_s$ at initial time $t = 0$. The corresponding velocity field is denoted $u_o(x)$, and we obtain the velocity potential from spatial integration

$$\phi_o(x) = \int u_o(\xi)d\xi. \tag{9}$$

After some algebra and by using the following notations

$$f(x) = e\tanh b(x - x_s) \quad \text{with} \quad e = \sqrt{\frac{A}{A + h}}, \tag{10}$$

we obtain

$$\phi_o(x) = -\frac{Ce}{2b}\log\frac{1 + f(x)}{1 - f(x)}. \tag{11}$$

As an example, Figure 2 shows the successive wave profiles starting from a soliton with initial amplitude $A = 0.18$ m.

Math. Meth. Appl. Sci. 2015, 38 2041–2052
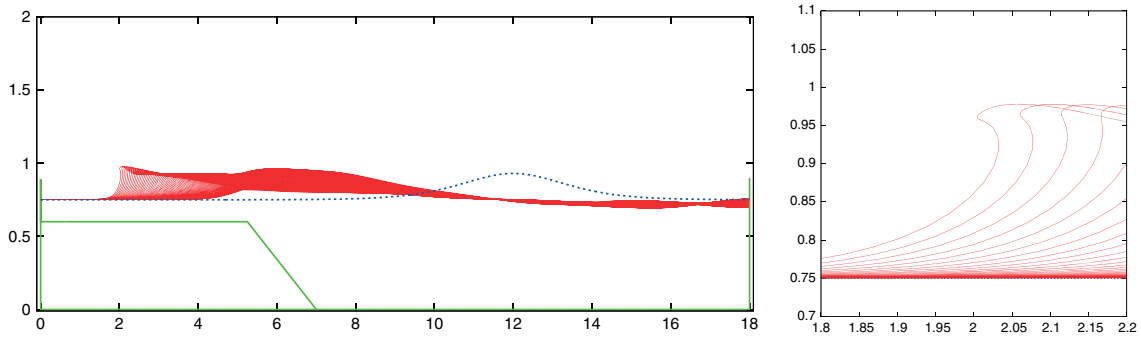
2043

Figure 2. Successive wave profiles starting from the solution, which represents a soliton traveling from right to left (in blue). The tank and the bathymetry are shown in green. The right figure is a close view of the overturning crest with the same scale in x and y.
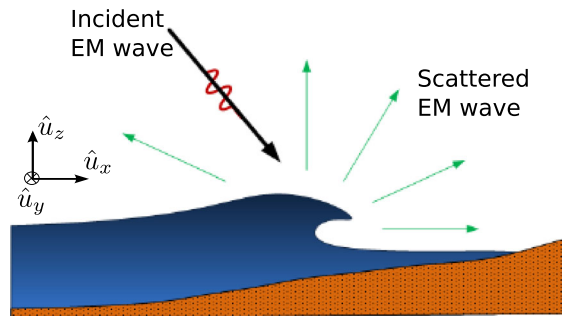

Figure 3. Electromagnetic scattering by a breaking sea wave.

3. Electromagnetic scattering

Because the profiles of the breaking sea waves can be numerically computed for different configurations by the here-presented hydrodynamic model, we want to estimate the electromagnetic field scattered by these profiles, see Figure 3.

For different angles of incidence, the electromagnetic modeling consists in the evaluation of the scattering of a plane wave by a dielectric interface. As a matter of fact, due to the salinity of the sea water, the surface is assumed to be a perfect electric conductor. Without loss of generality, any polarized plane wave can be split into two linear polarized plane waves: transverse magnetic (TM) and transverse electric (TE) polarization.

For solving open-region electromagnetic scattering problems, a very popular way to model the scattering by TM and TE polarized wave is to consider the boundary integral equation method.

For the TM polarization ($\mathbf{E} = E\hat{u}_y$), the modeling of the scattering is based upon the electric field integral equation [8]:

$$E_y^{inc}(\mathbf{r}) = i\omega_{em}\mu \int_\Gamma J_{TM}(\mathbf{r}')G(\mathbf{r},\mathbf{r}')\,d\mathbf{r}', \tag{12}$$

where E_y^{inc} is the incident field, μ is the permeability of free space, Γ represents the sea surface, ω_{em} is the angular frequency of the electromagnetic wave, J_{TM} is the surface current, $G(\mathbf{r},\mathbf{r}')$ is the 2D Green function of Helmholtz equation, and $\mathbf{r}' = (x',z')$ and $\mathbf{r} = (x,z)$ are the source and observation points on the sea surface ($\mathbf{r}', \mathbf{r} \in \Gamma$). It is worth noting that the incident wave is known and is assumed to be tapered to avoid numerical truncation effects. So, the amplitude E_y^{inc} of the incident field will be given by [9]:

$$E_y^{inc}(\mathbf{r}) = \underbrace{\exp\left(i\left(\mathbf{k_{inc}} \cdot \mathbf{r}\right)\right)}_{\text{plane wave}} \underbrace{\exp\left(-\frac{(x + z\tan\theta_i)^2}{g_t^2}\right)}_{\text{Gaussian}} \underbrace{F_{thor}(\mathbf{r})}_{\text{Thorsos factor}}, \tag{13}$$

where k_{inc} is the incident wave vector, θ_i is the angle of incidence, g_t is the tapering parameter, and the Thorsos factor is given by

$$F_{thor}(\mathbf{r}) = 1 + \frac{\left[2\frac{(x+z\tan\theta_i)^2}{g_t^2} - 1\right]}{(kg_t\cos\theta_i)^2}, \tag{14}$$

where k is the incident wave number.

The 2D Green function $G(\vec{r}, \vec{r}')$ is also perfectly known, and the only unknown function of the integral equation (12) is the surface current J_{TM}. When the surface current is computed, the scattered field is determined using the following relation:

$$E_y^{scat}(\mathbf{r}_{obs}) = -i\omega_{em}\mu \int_\Gamma J_{TM}(\mathbf{r}')G(\mathbf{r}_{obs}, \mathbf{r}')\, d\mathbf{r}', \tag{15}$$

where $\mathbf{r}_{obs}$ is the position of the observer above the sea surface.

For the TE polarization, the electrical field $\mathbf{E}$ belongs to the plane $(O, \hat{u}_x, \hat{u}_z)$, and the magnetic field is in the form $(\mathbf{H} = H_y\hat{u}_y)$. Then the modeling of the scattering in TE polarization is based upon the magnetic field integral equation [8]:

$$H_y^{inc}(\mathbf{r}) = -\frac{J_{TE}(\mathbf{r})}{2} + \int_\Gamma J_{TE}(\mathbf{r}')\left[\hat{n}(\mathbf{r}')\nabla'G(\mathbf{r}, \mathbf{r}')\right]d\mathbf{r}', \tag{16}$$

where $\hat{n}(\mathbf{r})$ is the normal vector to the sea surface at the position $\mathbf{r}$, $\nabla'G(\mathbf{r})$ is the gradient related to the second variable of the Green function, H_y^{inc} is the incident field, and J_{TE} is the surface current. In the same way as the TM polarization case, the integral equation (16) determines the surface current J_{TE}. So, the magnetic field $\mathbf{H}$ received by the observer is computed by using a relation similar to equation (15), and then the electric field received by the observer can be evaluated.

From a mathematical point of view, the boundary integral equation method, in both TM and TE polarization cases, boils down to a Fredholm integral equation of the first kind:

$$g(\mathbf{r}) = \int_\Gamma k(\mathbf{r}, \mathbf{r}')f(\mathbf{r}')\, d\mathbf{r}', \tag{17}$$

where $g(\mathbf{r})$ and $k(\mathbf{r}, \mathbf{r}')$ are known functions on the boundary Γ. It is worth noting that, because $\mathbf{r}, \mathbf{r}' \in \Gamma$, the Fredholm integral equation remains a one-dimensional problem. Letting $s \in [0, 1]$ a normalized curvilinear coordinate on Γ, we can write $\mathbf{r} = (x(s), y(s)) = \mathbf{r}(s)$ and $\mathbf{r}' = (x'(s), y'(s)) = \mathbf{r}'(s)$. The Fredholm integral equation becomes

$$g(\mathbf{r}(s)) = \int_0^1 k(\mathbf{r}(s), \mathbf{r}'(s'))f(\mathbf{r}'(s'))\sqrt{\left(\frac{dx'}{ds'}\right)^2 + \left(\frac{dy'}{ds'}\right)^2}\, ds'. \tag{18}$$

Or more simply

$$g(s) = \int_0^1 K(s, s')f(s')\, ds', \tag{19}$$

where K is an operator which only depends on the geometry of Γ.

A typical approach for solving integral equations is to approximate the solution with function basis:

$$f(x) \approx f_N(x) = \sum_{i=1}^N f_i\Psi_i(x). \tag{20}$$

For standard method of moments (MoM) [8, 10]), expansion functions $\Psi_i(x)$ are pulse basis functions or, in continuous cases (first order Sobolev space), are triangular basis functions, see Figure 4.

For smooth surfaces, standard method of moment (MoM) provides excellent numerical results for both TM and TE polarizations, where the resolution h is lower than the scale $\lambda/10$. Unfortunately, for more irregular surfaces with cavities or high local curvatures,
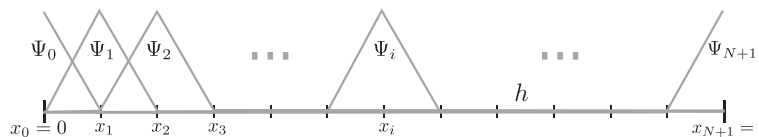
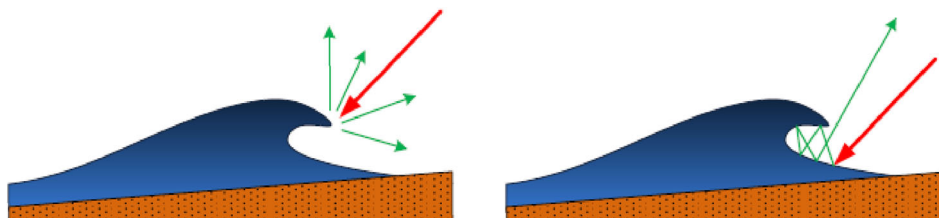**Figure 4.** Triangular basis functions $\Psi_i(x)$ between 0 and 1 ($h = x_{i+1} - x_i = 1/N$).

Figure 5. High curvature (crest) and cavity of a plunging breaking sea wave profile.

Math. Meth. Appl. Sci. **2015**, 38 2041–2052

2045

the length scale $\lambda/10$ is too great. In these cases, a standard MoM approach often faces serious problems concerning numerical convergence. For several canonical profiles, it has been shown that the loss of precision is directly related to an increase of curvature [11, 12], and this lack of precision almost always appears where local curvatures exist.

In our case, plunging breaking sea waves necessarily induce cavities and local curvature, see Figure 5 with complex electromagnetic interactions. More precisely, Figure 6 clearly stresses the peak of local curvature near the plunging wave crest. Under these circumstances, standard MoM requires a very high resolution ($\lambda/100$ or less) and involves huge systems of linear equations. Therefore, it seems logical to investigate alternative approaches.

In fact, the problem of numerical convergence to model the electromagnetic field scattered by a breaking wave is a well-known issue for the maritime remote sensing community. In previous studies, hybrid approaches [13, 14], combining MoM with ray theory and asymptotic approximation, or higher order MoM [15] were investigated, but they are only a partial solution to the problem. In the present study, we analyze the breaking wave profile with a multiscale point of view: high precision scale for the crest and low precision scale for the global shape of the profile. To avoid the boom in the complexity of systems generated by a multiscale method of moments, we apply an AMMM built on the work carried out by Su and Sarkar [16, 17].

3.1. Multiscale basis functions

Many studies in the 1990s [18–22] demonstrated the interest to use various multiscale basis functions for modeling. In this paper, multiscale basis functions are based on the standard triangular basis functions, as illustrated in Figure 4.

Let $f(x)$ be a real-valued function of a real variable. For the sake of simplicity, $f(x)$ is assumed to be defined between $x_{0,0} = 0$ and $x_{0,1} = 1$. A linear interpolation between $x_{0,0}$ and $x_{0,1}$ is given by

$$f_0(x) = f(x_{0,0})\,\phi_0(x) + f(x_{0,1})\,\phi_1(x), \tag{21}$$

where

$$\phi_0(x) = \phi_{0,1}(x) = \begin{cases} 1 - x & x \in [0, 1] \\ 0 & \text{otherwise} \end{cases} \tag{22}$$

and

$$\phi_1(x) = \phi_{0,2}(x-1) \qquad \phi_{0,2}(x) = \begin{cases} x + 1 & x \in [-1, 0[\\ 0 & \text{otherwise.} \end{cases} \tag{23}$$

This linear interpolation represents the zeroth approximation of the function $f(x)$. At this zeroth scale, the basis functions $\phi_0(x)$ and $\phi_1(x)$ are triangular basis functions.
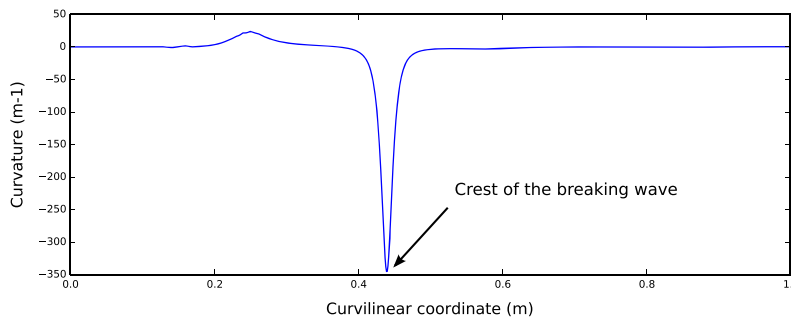

Figure 6. Curvature of the breaking wave profile as a function of the curvilinear coordinate.

(a) Triangular basis functions 1'st order   **(b)** Multiscale basis functions 1'st order
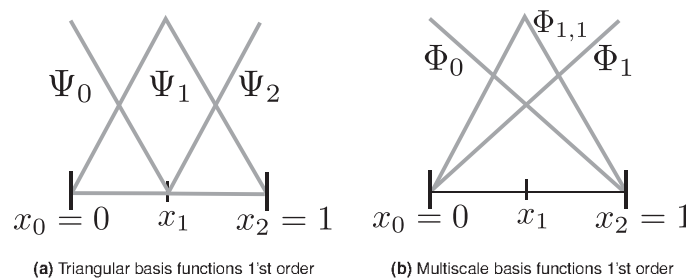
Figure 7. Basis function with $x_0 = 0$, $x_1 = x_{1,1}$, and $x_2 = 1$ at first order. (a) Triangular basis functions first order and (b) multiscale basis functions first order.

At the first scale, the midpoint $x_{1,1} = (x_{0,0} + x_{0,1})/2 = 1/2$ is taken into account for the interpolation, and the approximation is in the form

$$f_1(x) = f_0(x) + \tau_{1,1}\phi_{1,1}(x), \tag{24}$$

where $\phi_{1,1}(x) = (\phi_{0,1}[2(x - x_{1,1})] + \phi_{0,2}[2(x - x_{1,1})])$.
Assuming $f_1(x_{1,1}) = f(x_{1,1})$, we obtain

$$\tau_{1,1} = f(x_{1,1}) - f_0(x_{1,1}) = f(x_{1,1}) - \frac{1}{2}(f(x_{0,0}) + f(x_{0,1})). \tag{25}$$

Considering the three points $x_0 = 0$, $x_1 = x_{1,1}$, and $x_2 = 1$, the first scale basis functions are given by $\phi_0(x)$, $\phi_1(x)$, and $\phi_{1,1}(x)$, see Figure 7(b). It is clear that these first scale basis functions are no longer equivalent to the standard triangular basis, see Figure 7. Contrarily, to the standard triangular basis, this new basis associate two scales: zeroth scale with $\phi_0(x)$ and $\phi_1(x)$, and first scale with $\phi_{1,1}(x)$.

At first approximation, both basis (multiscale and triangular) are linearly related:

$$\Psi_1 = (\Psi_0, \Psi_1, \Psi_2)^T = T_1 \cdot (\Phi_0, \Phi_1, \Phi_{1,1})^T = T_1 \cdot \Phi_1 \qquad \text{where} \qquad T_1 = \begin{pmatrix} 1 & 0 & -1/2 \\ 0 & 0 & 1 \\ 0 & 1 & -1/2 \end{pmatrix}. \tag{26}$$

At the second scale, two new points $x_{2,1} = (x_{0,0} + x_{1,1})/2 = 1/4$ and $x_{2,2} = (x_{1,1} + x_{0,1})/2 = 3/2$ are taken into account, and a second order approximation can be defined:

$$f_2(x) = f_1(x) + \tau_{2,1}\phi_{2,1}(x) + \tau_{2,2}\phi_{2,2}(x), \tag{27}$$

where $\phi_{2,1}(x) = (\phi_{0,1}[2^2(x - x_{2,1})] + \phi_{0,2}[2^2(x - x_{2,1})])$ $\phi_{2,2}(x) = (\phi_{0,1}[2^2(x - x_{2,2})] + \phi_{0,2}[2^2(x - x_{2,2})])$. In the same way as for the first order, we assume that $f_2(x_{2,1}) = f(x_{2,1})$ and $f_2(x_{2,2}) = f(x_{2,2})$. It obviously follows therefore that

$$\tau_{2,1} = f(x_{2,1}) - f_1(x_{2,1}) = f(x_{2,1}) - \frac{1}{2}(f(x_{0,0}) + f(x_{1,1})) \tag{28}$$

$$\tau_{2,2} = f(x_{2,2}) - f_1(x_{2,2}) = f(x_{2,2}) - \frac{1}{2}(f(x_{1,1}) + f(x_{0,1})) \tag{29}$$

Now, considering the points $x_0 = 0$, $x_1 = x_{2,1}$, $x_2 = x_{1,1}$, $x_3 = x_{2,2}$, and $x_4 = 1$, the multiscale basis functions are a combination of two zeroth scale functions ($\phi_0(x)$ and $\phi_1(x)$), a first scale function ($\phi_{1,1}(x)$), and two second scale functions ($\phi_{2,1}(x)$ and $\phi_{1}2,2(x)$). Unlike the triangular basis functions, they are not limited to one scale, see Figure 8.

At second approximation, both bases (multiscale and triangular) are linearly related:

$$\Psi_2 = (\Psi_0, \Psi_1, \Psi_2, \Psi_3, \Psi_4)^T = T_2 \cdot (\Phi_0, \Phi_1, \Phi_{1,1}, \Phi_{2,1}, \Phi_{2,2})^T = T_2 \cdot \Phi_2, \tag{30}$$

where

$$T_2 = \begin{pmatrix} 1 & 0 & -1/2 & -1/2 & 0 \\ 0 & 0 & 0 & 1 & 0 \\ 0 & 0 & 1 & -1/2 & -1/2 \\ 0 & 0 & 0 & 0 & 1 \\ 0 & 1 & -1/2 & 0 & -1/2 \end{pmatrix}. \tag{31}$$
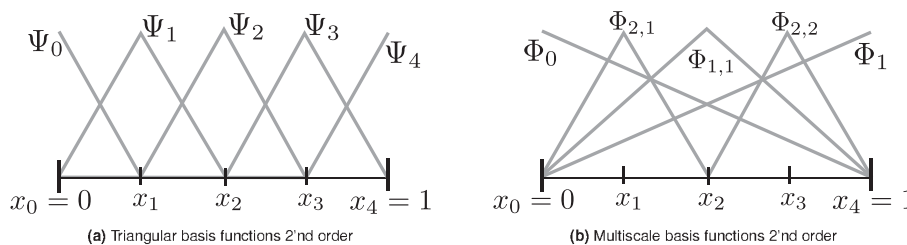

(a) Triangular basis functions 2'nd order

(b) Multiscale basis functions 2'nd order

Figure 8. Basis function with $x_0 = 0$, $x_1 = x_{2,1}$, $x_2 = x_{1,1}$, $x_3 = x_{2,2}$, and $x_4 = 1$ at second order.

Math. Meth. Appl. Sci. **2015**, 38 2041–2052
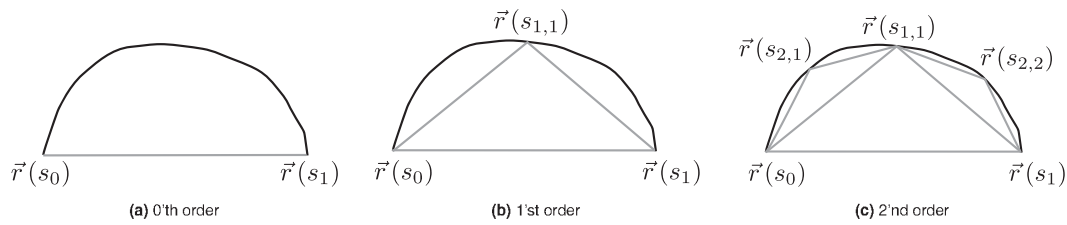
2047

Figure 9. Multiscale parametric curvilinear midpoints at zeroth, first, and second order.

These multiscale basis functions can be generalized to any Jth scale by recursively introducing new points $\left\{x_{J,i} = \frac{1}{2^J} + \frac{i-1}{2^{J-1}}, i = 1, 2, \cdots, 2^{J-1}\right\}$ and by considering Jth order approximation:

$$f_J(x) = f_{J-1}(x) + \sum_{i=1}^{2^{J-1}} \tau_{J,i} \phi_{J,i}(x) = f_0(x) + \sum_{j=1}^{J} \sum_{i=1}^{2^{J-1}} \tau_{j,i} \phi_{j,i}(x), \tag{32}$$

where $\phi_{j,i}(x) = \left(\phi_{0,1}\left[2^j(x - x_{j,i})\right] + \phi_{0,2}\left[2^j(x - x_{j,i})\right]\right)$. As previously, letting $f_J(x_{J,i}) = f(x_{J,i})$, $i = 1, 2, \cdots, 2^{J-1}$, we obtain an explicit expression of functions $\tau_{J,i}$:

$$\tau_{J,i} = f(x_{J,i}) - f_{J-1}(x_{J,i}) = f(x_{J,i}) - f_0(x_{J,i}) - \sum_{j=1}^{J-1} \sum_{i=1}^{2^{J-2}} \tau_{j,i} \phi_{j,i}(x_{J,i}) = f(x_{J,i}) - \frac{1}{2}\left(f\left(x_{J,i} - \frac{1}{2^J}\right) + f\left(x_{J,i} - \frac{1}{2^J}\right)\right). \tag{33}$$

In the case of a 2D parametric curve, this iterative division process does not raise any particular issue. From a geometric point of view, the recursive midpoint with the curvilinear coordinate s may be understood as intermediate points on the curve $s_{J,i} \longmapsto \mathbf{r}(s_{J,i})$, see Figure 9. The linear multiscale basis functions of the variable s can be easily obtained with any parametric curve in 2D. Thus, they can be applied to the profiles of the breaking sea waves.

In practice, at the zeroth scale, nodal points are an equally spaced set of $N + 1$ points $\left\{s_{0,i} = \frac{i}{N}; i = 0, 1, ..., N\right\}$, and zeroth scale basis functions are triangular functions given by

$$\phi_0(s) = \phi_{0,1}(s), \qquad \phi_N(s) = \phi_{0,2}(s - 1) \quad \text{and} \quad \phi_i(s) = \left(\phi_{0,1}(s - s_{0,i}) + \phi_{0,2}(s - s_{0,i})\right), \tag{34}$$

where $i = 1, 2, \cdots, N - 1$ and

$$\phi_{0,1}(s) = \begin{cases} 1 - sN & s \in [0, h] \\ 0 & otherwise \end{cases} \quad \text{and} \quad \phi_{0,2}(s) = \begin{cases} 1 + s \times N & s \in [-h, 0[\\ 0 & otherwise. \end{cases} \tag{35}$$

At the zeroth order, function $f(s)$ approximation is

$$f_0(s) = \sum_{n=0}^{N} f(s_{0,n}) \phi_n(s). \tag{36}$$

Using the previously presented iterative method, the Jth order approximation is in the form

$$f_J(s) = \sum_{n=0}^{N} f(s_{0,n}) \phi_n(s) + \sum_{j=1}^{J} \sum_{i=1}^{2^{j-1}N} \tau_{j,i} \phi_{j,i}(s), \tag{37}$$

where $\left\{s_{j,i} = \frac{1}{2^j N} + \frac{i-1}{2^{j-1}N}, i = 1, 2, \cdots, 2^{j-1}N\right\}$, $\phi_{j,i}(s) = \left(\phi_{0,1}(2^j(s - s_{j,i})) + \phi_{0,2}(2^j(s - s_{j,i}))\right)$, and

$$\tau_{j,i} = f(s_{j,i}) - \frac{1}{2}\left(f\left(s_{j,i} - \frac{1}{2^j N}\right) + f\left(s_{j,i} + \frac{1}{2^j N}\right)\right). \tag{38}$$

Finally, the main problem is to develop an efficient method of moments based upon these multiscale basis functions $\left\{\Phi_i(s), \Phi_{j,k}(s)\right\}$.

3.2.   Adaptive multiscale method of moments

At Jth order, Su and Sarkar [23] showed that the method of moment using $\{\Phi_i(s), \Phi_{j,k}(s)\}$ as weight and testing functions for the Fredholm integral equation (19) leads to the following linear system:

$$\begin{pmatrix} F_0 \\ F_1 \\ \vdots \\ F_J \end{pmatrix} = \begin{pmatrix} A_{0,0} & A_{0,1} & \cdots & A_{0,J} \\ A_{1,0} & A_{1,1} & \cdots & A_{1,J} \\ \vdots & \vdots & \ddots & \vdots \\ A_{J,0} & A_{J,1} & \cdots & A_{J,J} \end{pmatrix} \cdot \begin{pmatrix} X_0 \\ X_1 \\ \vdots \\ X_J \end{pmatrix}, \tag{39}$$

where $X_0 = (\tau_{0,0}, \tau_{0,1}, \cdots, \tau_{0,N})^T$ and $X_j = (\tau_{j,1}, \cdots, \tau_{j,2^{j-1}N})^T$. F_j and $A_{j,l}$ are known integrals explicitly described in [23].

The authors suggest to solve this linear system using a recursive scheme. First, the linear at the zeroth order $A_{0,0}X_0 = F_0$ is considered, an iterative linear system solver provides the estimated solution X_0^{*0}. Then, beginning with the point $(X_0^{*0}, 0)$, the iterative process estimates the solution of the linear system:

$$\begin{pmatrix} F_0 \\ F_1 \end{pmatrix} = \begin{pmatrix} A_{0,0} & A_{0,1} \\ A_{1,0} & A_{1,1} \end{pmatrix} \cdot \begin{pmatrix} X_0 \\ X_1 \end{pmatrix}. \tag{40}$$

The so-obtained estimated solution is denoted (X_0^{*1}, X_1^{*0}). Finally, assuming that the estimated solution $(X_0^{*i}, X_1^{*i-1}, \cdots, X_i^{*0})$ is known at the ith order, the iterative solver beginning with the point $(X_0^{*i}, X_1^{*i-1}, \cdots, X_i^{*0}, 0)$ can estimate the solution $(X_0^{*i+1}, X_1^{*i}, \cdots, X_i^{*1}, X_{i+1}^{*0})$ at the i+1th order, and so on until the final linear equation (40) at the Jth order. In practice, we find that the beginning points are always in the basin of attraction of the solution, and the iterative solver converges very quickly. In the present study, we apply the generalized minimal residual method [24] for our computations.

At each step, the solver provides an approximation at the ith order. Using an interpolation (spline interpolation for instance), this functional approximation can roughly approximate all the coefficients $\tau_{i+1,.}$. If the norm of a coefficient $\tau_{i+1,.}$ is lower than a predetermined minimum threshold, the coefficient can be arbitrarily set to 0, and the corresponding line of the linear system is removed. With such a specific threshold, this method induces a drastic reduction of the dimensionality. In this way, we obtain an AMMM that can be applied to evaluate the electromagnetic scattered by a breaking sea wave.

4. Numerical simulation

Following the general formalism described in [23], F_j and $A_{j,l}$ respectively involve 1D and 2D numerical integration. Within the context of electromagnetic scattering simulation, these integrals are highly oscillating where the domain of integration is much larger than
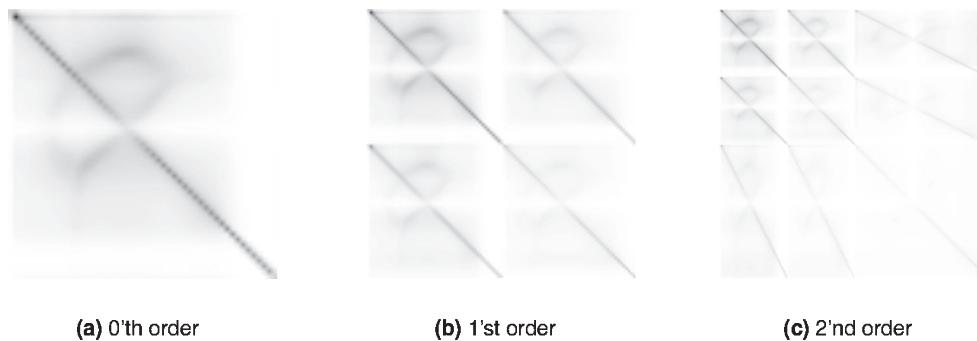

(a) 0'th order   **(b)** 1'st order   **(c)** 2'nd order

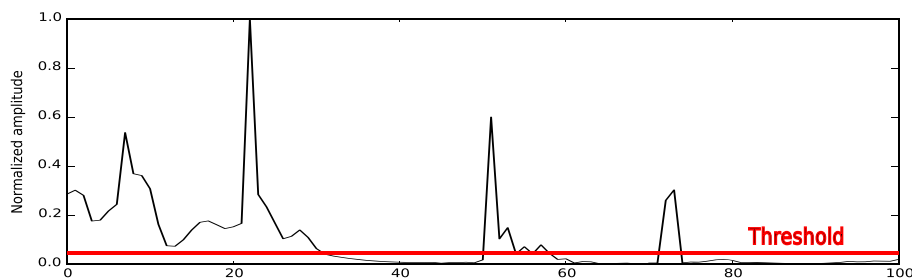**Figure 10.** Absolute value of the matrix A at zeroth, first, and second order.

Figure 11. Normalized distribution of **X** (the first 100 elements) for transverse magnetic polarization with an angle of incidence set at 45°.

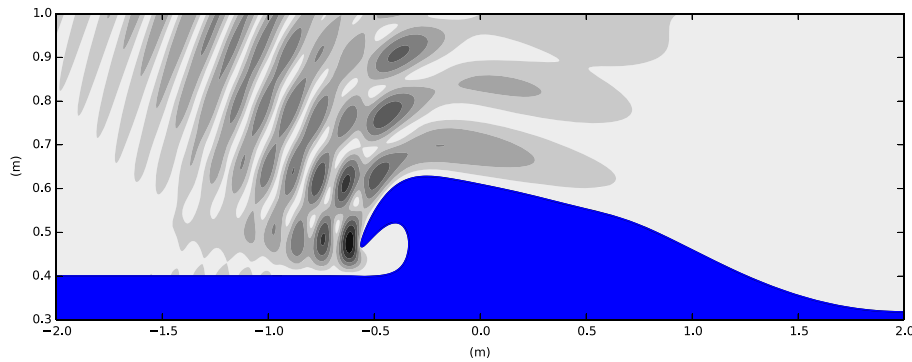*Math. Meth. Appl. Sci.* **2015**, 38 2041–2052

2049

Figure 12. Total electromagnetic field (incident+scattered) estimated at the sixth order with an angle of incidence set at 45° in transverse magnetic polarization.
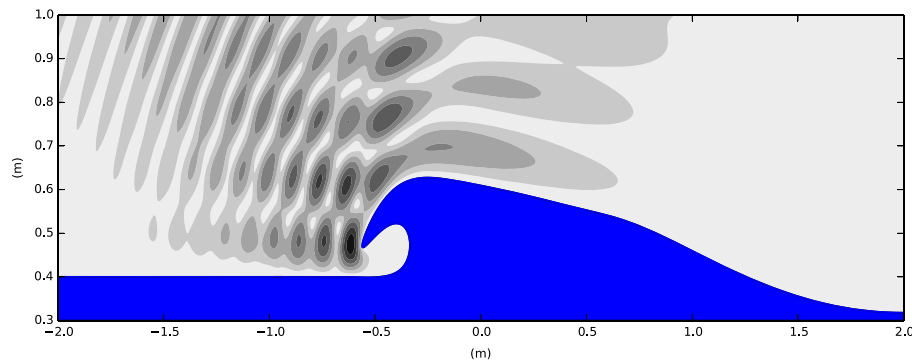

Figure 13. Total electromagnetic field (incident+scattered) computed by standard method of moments (10000 elements) with an angle of incidence set at 45° in transverse magnetic polarization.

electromagnetic wavelength λ_{em} and raise severe convergence problems. In the present case, the electromagnetic frequency is set to $f_{em} = 1.5\,10^9$ Hz and $\lambda_{em} = 20$ cm. At the zeroth order, N is chosen such that the domain of integration is lower than $\lambda_{em}/2$. Figure 10 shows the absolute value of the coefficient $A_{j,l}$ for the first three orders. We clearly see that the matrix A is a symmetric matrix. This is due to the fact that in our model, $k\,(s,s')$ is a symmetric function $k\,(s,s') = k\,(s',s)$. Moreover, the multiscale structure of the matrix A is clearly illustrated in Figure 10.

Assuming the matrix A as known, we compute the vector F for a given angle of incidence, and by solving the linear equation system (recursive generalized minimal residual method), we obtain the vector $\left(X_0^{*i+1}, X_1^{*i}, \cdots, X_i^{*1}, X_{i+1}^{*0} \right)$. As shown in Figure 11, the elements of this vector globally decrease if the order increases. However, there are specific peaks that mainly correspond to rapid fluctuations, near the crest of the sea wave for instance. The great amplitude variation between these peaks and the rest of the curve is the reason why we can apply a drastic reduction of the dimensionality using a threshold. In the present case, at the sixth order, the ratio between the theoretical dimension and the actual one if small values are neglected can be lower than 10% while maintaining good computational quality.

Finally, AMMM makes it possible to calculate the electromagnetic field scattered by a breaking wave with any angle of incidence. In Figure 12, the incident angle is set to $+45°$, and we can notice the good level of detail for the estimated electromagnetic field in the vicinity of the sea wave crest. In order to compare this simulation with a reliable reference, a 'brute-force' approach was employed. More precisely, Figure 13 presents the same simulation obtained by a standard MoM with a huge number of element. As we can see, the two simulations give similar results; however, the dimension of the MoM linear system is more than ten times higher than the AMMM linear system.

Same kind of simulations has been made for normal incidence and with incident angle set to $-45°$, see Figures 14 and 15.

Much more than numerical precision of the computation, it is important to underline that AMMM is a good tool to analyze the scattering phenomenon at different scales. In this study, the contrast between the peaks of the sea wave and the smoother part of the curve becomes very clear if we consider the distribution of the vector $\left(X_0^{*i+1}, X_1^{*i}, \cdots, X_i^{*1}, X_{i+1}^{*0} \right)$ at different orders.

Despite many advantages of the AMMM to simulate the scattering by profiles with high local curvatures, it is worth to underline that AMMM requires a good precision for the coefficients of the matrix $A_{j,l}$. The components of this matrix correspond to numerical estimations of double integrals. To obtain a good precision with AMMM, the reliable estimation of these components is often paid with quite long computation times. This is the reason why the computation of double integrals must be very optimized to obtain a global saving of time if AMMM is used. In this article, we applied Gaussian quadrature algorithm for numerical integration, and we did not saved much time as compared with standard MoM. However, one can certainly expect significant progress to speed up AMMM algorithm, using parallel computing for instance.
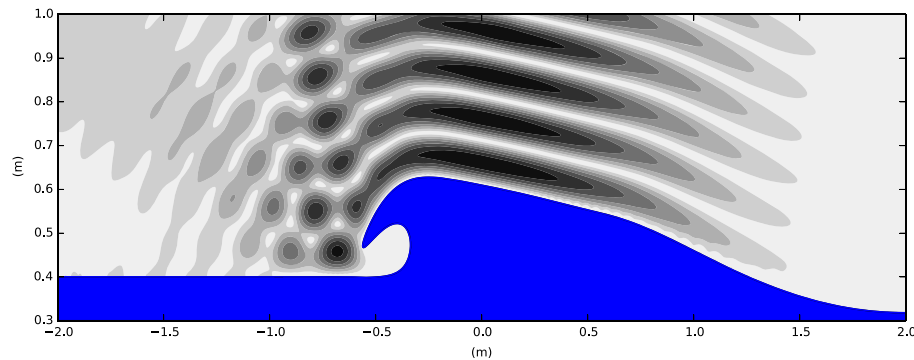
Figure 14. Total electromagnetic field (incident+scattered) estimated at the sixth order with an angle of incidence set at $0°$ in transverse magnetic polarization.
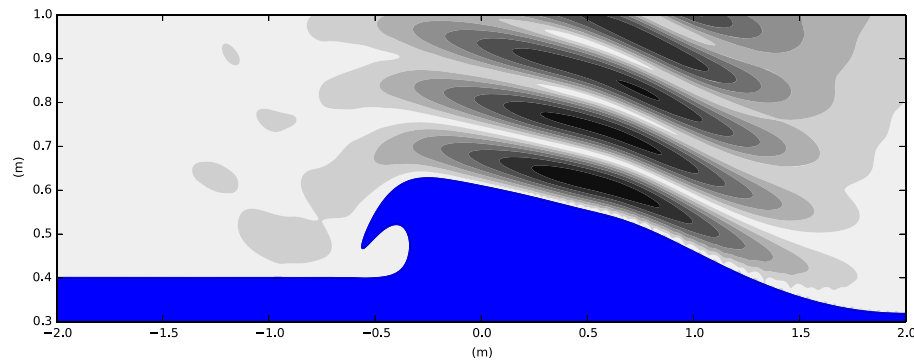

Figure 15. Total electromagnetic field (incident+scattered) estimated at the sixth order with an angle of incidence set at $-45°$ in transverse magnetic polarization.

5. Conclusion

At the pragmatic level, we show in this article that the combination of two mathematical models related to hydrodynamics and electromagnetics can be used to simulate a complex multiphysic phenomenon. With regard to the hydrodynamic model, our original approach avoids the great computational complexity of other standard methods. From the electromagnetic point of view, we have shown that, for maritime remote sensing application, AMMM provides a credible alternative to a standard MoM based on a 'brute-force' approach. In particular, we have highlighted the fact that AMMM can accurately simulate the electric field near the crest of breaking waves (high local curvature). This multiscale approach opens the way toward a close analysis of the scattering by local curvatures and cavities. In this sense, this method will probably makes easier the physical interpretation of the interaction between electromagnetic waves and nonlinear sea waves.

References

1. Ayari Y, Khenchaf A, Coatanhay A. Bistatic scattering by sea surface at large incident angles: two scale model using the unified sea spectrum. *Journal of Applied Remote Sensing* 2007; **1**(013532):1–19.
2. Awada A, Ayari MY, Khenchaf A, Coatanhay A. Bistatic scattering from an anisotropic sea surface: numerical comparison between the first-order SSA and the TSM models. *Waves in Random and Complex Media* 2006; **16**(3):383–394.
3. Warnick KF, Chew WC. Numerical simulation methods for rough surface scattering. *Waves in Random Media* 2001; **11**(1):R1—R30.
4. Ma Q (ed). *Advances in Numerical Simulation of Nonlinear Water Waves*. World Scientific: London (UK), 2010.
5. Wang P, Yao Y, Tulin MP. An efficient numerical tank for non-linear water waves, based on the multi-subdomain approach with bem. *International Journal for Numerical Methods in Fluids* 1995; **20**(12):1315–1336.
6. Scolan YM. Some aspects of the flip-through phenomenon: a numerical study based on the desingularized technique. *Journal of Fluids and Structures* 2010; **26**:918–953.
7. Mei CC. *The Applied Dynamics of Ocean Surface Waves*. Wiley-Interscience: Singapore, 1983.
8. Gibson W. *The Method of Moments in Electromagnetics*. Chapman & Hall/CRC: Boca Raton (USA), 2008.
9. Thorsos EI. The validity of the kirchhoff approximation for rough surface scattering using a Gaussian roughness spectrum. *Journal of the Acoustical Society of America* 1988; **83**(1):78–92.
10. Tsang L, Kong JA, Ding K-H, Ao CO. *Scattering of Electromagnetic Waves: Numerical Simulations*. John Wiley & Sons: New York (USA), 2001.
11. Davis CP, Warnick KF. Error analysis of 2-D MoM for MFIE/EFIE/CFIE based on the circular cylinder. *IEEE Transactions on Antennas and Propagation* 2005; **53**:321–331.

12. Khairi R, Coatanhay A, Khenchaf A. Optimal high-order method of moment combined with NURBS for the scattering by a 2D cylinder. *Advanced Electromagnetics* 2013; **2**(1):33–43.

13. West JC. Low-grazing scattering from breaking water waves using an impedance boundary MM/GTD approach. *IEEE Transactions on Antennas and Propagation* 1998; **46**:93–100.

14. West JC. Low-grazing-angle (LGA) sea-spike backscattering from plunging breaker crests. *IEEE Transactions on Geoscience and Remote Sensing* 2002; **40**:523–526.

15. Khairi R, Coatanhay A, Khenchaf A, Scolan Y-M. Numerical modeling of electromagnetic waves scattering from 2D coastal breaking sea waves. *The European Physical Journal Applied Physics* 2013; **64**(2):24505–24510.

16. Su C, Sarkar TK. Adaptive multiscale moment method (AMMM) for analysis of scattering from perfectly conducting plates. *IEEE Transactions on Antennas and Propagation* 2000; **48**(6):932–939.

17. Su C, Sarkar TK. Adaptive multiscale moment method (AMMM) for analysis of scattering from three-dimensional perfectly conducting structures. *IEEE Transactions on Antennas and Propagation* 2002; **50**(4):444–450.

18. Beylkin G, Coifman R, Rokhlin V. Fast wavelet transform and numerical algorithm I. *Communications on Pure and Applied Mathematics* 1991; **44**: 141–183.

19. Alpert BK, Beylkin G, Coifman R, Rokhlin V. Wavelet-like bases for the fast solution of second-kind integral equation. *SIAM Journal of Scientific Computing* 1993; **14**:159–184.

20. Steinbery BZ, Leviatan Y. On the use of wavelet expansions in the method of moments. *IEEE Transactions on Antennas and Propagation* 1993; **41**(5):610–619.

21. Goswani JC, Chan AK, Chui CK. On moments first-kind integral equations using wavelets on a bounded interval. *IEEE Transactions on Antennas and Propagation* 1995; **43**(6):614–622.

22. Wang G. A hybrid wavelet expansion and boundary element analysis of electromagnetic scattering from conducting objects. *IEEE Transactions on Antennas and Propagation* 1995; **43**(2):170–178.

23. Su C, Sarkar TK. A multiscale moment method for solving Fredholm integral equation of the first kind. *PIER* 1997; **17**:237–264.

24. Saad Y. *Iterative Methods for Sparse Linear Systems* 2nd ed. Society for Industrial and Applied Mathematics: Philadelphia (USA), 2003.